UCSF
UC San Francisco Previously Published Works

Title
Strain-guided mineralization in the bone-PDL-cementum complex of a rat periodontium.

Permalink
https://escholarship.org/uc/item/3xk421vb

Authors
Grandfield, Kathryn
Herber, Ralf Peter
Chen, Ling
et al.

Publication Date
2015-12-01

DOI
10.1016/j.bonr.2015.04.002

Peer reviewed

eScholarship.org Powered by the California Digital Library
University of California

Bone Reports 3 (2015) 20–31

Contents lists available at ScienceDirect

Bone Reports

journal homepage: www.elsevier.com/locate/bonr

Strain-guided mineralization in the bone–PDL–cementum complex of a rat periodontium

Kathryn Grandfield [a,1], Ralf-Peter Herber [b,1], Ling Chen [a], Sabra Djomehri [a], Caleb Tam [a], Ji-Hyun Lee [a], Evan Brown [a], Wood R. Woolwine III [a], Don Curtis [a], Mark Ryder [c], Jim Schuck [d], Samuel Webb [e], William Landis [f], Sunita P. Ho [a,*]

[a] Division of Biomaterials and Bioengineering, Department of Preventive and Restorative Dental Sciences, University of California San Francisco, San Francisco, CA 94143, United States
[b] Division of Orthodontics, Department of Orofacial Sciences, University of California San Francisco, San Francisco, CA 94143, United States
[c] Division of Periodontics, Department of Orofacial Sciences, University of California San Francisco, San Francisco, CA 94143, United States
[d] Materials Science Division, The Molecular Foundry, Lawrence Berkeley National Laboratory, Berkeley, CA 94720, United States
[e] Stanford Synchrotron Radiation Lightsource, SLAC National Accelerator Laboratory, Menlo Park, CA 94025, United States
[f] Department of Polymer Science, The University of Akron, OH 44325, United States

ARTICLE INFO

Article history:
Received 3 January 2015
Received in revised form 25 March 2015
Accepted 13 April 2015
Available online 18 April 2015

Keywords:
Mineralization
Adaptations
Bone–periodontal ligament–tooth complex
Mechanical strain
Interfaces
Attachment sites

ABSTRACT

Objective: The objective of this study was to investigate the effect of mechanical strain by mapping physicochemical properties at periodontal ligament (PDL)–bone and PDL–cementum attachment sites and within the tissues per se.

Design: Accentuated mechanical strain was induced by applying a unidirectional force of 0.06 N for 14 days on molars in a rat model. The associated changes in functional space between the tooth and bone, mineral forming and resorbing events at the PDL–bone and PDL–cementum attachment sites were identified by using micro-X-ray computed tomography (micro-XCT), atomic force microscopy (AFM), dynamic histomorphometry, Raman microspectroscopy, and AFM-based nanoindentation technique. Results from these analytical techniques were correlated with histochemical strains specific to low and high molecular weight GAGs, including biglycan, and osteoclast distribution through tartrate resistant acid phosphatase (TRAP) staining.

Results: Unique chemical and mechanical qualities including heterogeneous bony fingers with hygroscopic Sharpey's fibers contributing to a higher organic (amide III — 1240 cm^{-1}) to inorganic (phosphate — 960 cm^{-1}) ratio, with lower average elastic modulus of 8 GPa versus 12 GPa in unadapted regions were identified. Furthermore, an increased presence of elemental Zn in cement lines and mineralizing fronts of PDL–bone was observed. Adapted regions containing bony fingers exhibited woven bone-like architecture and these regions rich in biglycan (BGN) and bone sialoprotein (BSP) also contained high-molecular weight polysaccharides predominantly at the site of polarized bone growth.

Conclusions: From a fundamental science perspective the shift in local properties due to strain amplification at the soft–hard tissue attachment sites is governed by semiautonomous cellular events at the PDL–bone and PDL–cementum sites. Over time, these strain-mediated events can alter the physicochemical properties of tissues per se, and consequently the overall biomechanics of the bone–PDL–tooth complex. From a clinical perspective, the shifts in magnitude and duration of forces on the periodontal ligament can prompt a shift in physiologic mineral apposition in cementum and alveolar bone albeit of an adapted quality owing to the rapid mechanical translation of the tooth.

© 2015 The Authors. Published by Elsevier Inc. This is an open access article under the CC BY-NC-ND license (http://creativecommons.org/licenses/by-nc-nd/4.0/).

1. Introduction

The periodontal ligament (PDL) is vascularized and innervated softer structural component that assumes the role of regulating functional loads in the tooth–PDL–bone fibrous joint. While this joint is optimally engineered by nature to transfer loads and maintain tissues for function, it is also exposed to the inevitable parafunction, that is, exacerbated forces in the form of bruxism, jaw clenching, nail biting,

* Corresponding author at: Division of Biomaterials and Bioengineering, Department of Preventive and Restorative Dental Sciences, 707 Parnassus Avenue, University of California, San Francisco, CA 94143, United States.
E-mail address: sunita.ho@ucsf.edu (S.P. Ho).
[1] Both authors contributed equally.

http://dx.doi.org/10.1016/j.bonr.2015.04.002
2352-1872/© 2015 The Authors. Published by Elsevier Inc. This is an open access article under the CC BY-NC-ND license (http://creativecommons.org/licenses/by-nc-nd/4.0/).

altered loads resulting from hardness variation in diet intake, and/or through clinical interventions such as the application of orthodontic appliances. The common denominator and a notable factor for the aforementioned conditions include eccentrically placed mechanical loads (Jang et al., 2014; Lin et al., 2013). Biomechanically, an optimal PDL-space is thought to permit the redistribution and transfer of loads from the tooth to alveolar bone specifically when loads are placed along the axis of the bone–tooth complex. This configuration constitutes a concentric loading system, which most often in nature prompts an optimum function when loaded within physiological limits. It is thought that the resulting optimum PDL-space enables force transfer across the mineralized tissues of this complex organ. Hence the PDL-space along with the PDL has also been suggested to act as a vital construct along which alveolar bone remodels/models (Beertsen et al., 1997), with the potential for cementum formation and resorption to also occur. Therefore, an improved knowledge of the "mechano-responsive" nature of the PDL, specifically at the PDL–bone and PDL–cementum attachment sites is relevant to understanding the strain-induced responses to our clinical interventions. Mechanical forces exert strains at the attachment sites and can "turn on" cell-surface receptors and consequently a cascade of biochemical signals, which in turn cause mineral formation and resorption related events in bone and/or cementum.

There exist many clinical interventions in skeletal (distraction osteogenesis), and oral and craniofacial orthopedics (for example, cranial grafts, orthodontics) that involve the use of mechanical forces to "mold" and/or regenerate bone and subsequently its adjacent tissues. However, very little is known about the influence of mechanical stimulus on the biomineralization of tissues per se within the bone–PDL–tooth complex or the functional interfaces between the ligament–bone and ligament–cementum. The current doctrine regarding the role of PDL in response to applied loads has been summarized as: 1) the PDL distributes applied loads to the alveolar bone, 2) the direction, frequency, duration and magnitude of loading determine both the extent, rate of bone remodeling and quality of modeled bone, 3) the absence of PDL severely limits the extent of bone remodeling (Beertsen et al., 1997). In this study, we propose that the mechanoresponsive activity at the PDL–bone and PDL–cementum attachment sites responds to eccentric loading by mineral formation and/or resorption at these sites by altering the functional space between the tooth and bone.

The importance of functional adaptations of the bone, in particular at interfaces, is not limited to orthodontics, but extends into the orthopedics. Within orthopedics, it has been suggested that functional adaptation of the bone results from cellular responses to strain density within a softer matrix (Carter et al., 1987). In this study, we identify the effects of perceived unidirectional forces on mineralization within the bone–PDL–tooth joint, and specifically at the soft–hard tissue interfaces of the PDL–bone and PDL–cementum sites and correlate it to the cellular and tissue adaptations in a rat model. The specific sites that were mechanically stimulated included the PDL–bone and the PDL–cementum functional attachment sites. Due to the nature of the ligament–bone interfaces in the musculoskeletal system, including the ligament–cementum interfaces in the bone–PDL–tooth complex, i.e. disparate tissues interfacing over a distance of 10 μm, these sites are mechanically strained (Lu and Thomopoulos, 2013; Qian et al., 2009) and the rate of adaptation at the interfaces is higher compared to other modeling sites. Furthermore, the attachment sites present themselves as excellent model systems where mechano-responsiveness, i.e. the response of mechanical strain amplification on mineral formation and resorption can be investigated and better understood. However, based on literature, mechano-responsiveness is assumed to occur at two different sites, the soft–hard tissue attachment site per se, and 5 μm inwards defined as an interface where the soft tissue transitions into a harder tissue.

Fundamentally, from a structural engineering perspective, eccentric loads are thought to accentuate strains, specifically at regions where dissimilar materials are attached. This concept was examined in this study, where strains at the functional interfaces and attachment sites of the PDL–bone and PDL–cementum were amplified by placing an eccentric load on the periodontium of a rat for fourteen days. In particular, cellular morphological phenotype and tissue adaptations were correlated to matrix structure, mechanical properties, and biochemical and elemental compositions facilitated through various techniques, including immunohistochemistry, microcomputed X-ray tomography (micro-XCT), microprobe X-ray fluorescence (micro-XRF), micro Raman spectroscopy and nanoindentation. The importance of this study lies in complementary higher-resolution imaging techniques combined with conventional histological and immunohistochemical measures allowing an understanding of the effect of mechanical strains at the interfaces of the bone–PDL–tooth complex. Thus, the objective of this study is to investigate gross morphological changes within tissues of the bone–PDL–cementum complex, changes in architecture and physicochemical characteristics of the formed structures due to amplified strain at the PDL–bone attachment site and interface.

2. Materials & methods

Please see appendix for details on the animal model used in this study (Fig. S1). In brief, 60 cN of force was applied to molars and incisors of 4 month old male Sprague–Dawley rats (Charles River Laboratories International Inc., Wilmington, MA, USA). Following 14 days of mechanical stimulus, the specimens (N = 16, 8 experimental and 8 in control group) were harvested and prepared for further characterization. The study was conducted according to the regulations of the animal protocol AN080608-02, approved by the Institutional Animal Care and Use Committee (IACUC), University of California, San Francisco (UCSF).

2.1. Micro X-ray computed tomography (Micro-XCT™)

Entire dissected and fixed maxillae from experimental animals (N = 8) and control animals (N = 8) were placed in 70% ethanol, and were imaged at 2× magnification at 90 kVp, a power of 6 W and a camera binning of 2 using a Micro XCT-200 (micro-XCT, Xradia Inc., Pleasanton, CA, USA). For imaging of bone forming areas, magnification was increased to 10× and 20×. Exposure times were adjusted to yield 25% of the original X-ray intensity passing through the specimen and arriving at the detector. Tomographies were reconstructed (XMReconstructor, Version 7.0.2817, Xradia Inc., Pleasanton, CA, USA) and post-processed using the Xradia 3D viewer and Avizo® Fire 7.1 for 3D segmentation (Visage Imaging Inc., Version 5.2.2, San Diego, CA, USA).

The tomograms were also used to calculate volumes including bone volume (BV) and canal volume (Ca.V), and tissue volume (TV) based on previous works (Carter et al., 2013; Cooper et al., 2006; Parfitt et al., 1987). To note, "tissue volume" is referred to as "total volume" in this work, and is a sum of the BV and CV.

2.2. Histology and histochemistry

The appliance was removed and the specimens were cut into blocks consisting of the molars, PDL, and alveolar bone, only. After scanning with micro-XCT, the hemimaxillae were decalcified with ethylenediaminetetraacetic acid (EDTA) solution for 3 weeks. The decalcified specimens were dehydrated with 80%, 95% and 100% Flex alcohol (Richard-Allan Scientific, Kalamazoo, MI) before embedding in paraffin (Tissue Prep-II, Fisher Scientific, Fair Lawn, NJ). The paraffin blocks were sagittally sectioned on a rotary microtome (Reichert-Jung Biocut, Vienna, Austria) using a disposable steel blade (TBF Inc., Shur/Sharp, Fisher Scientific, Fair Lawn, NJ). The paraffin serial sections were mounted on Superfrost Plus microscope slides (Fisher Scientific, Fair Lawn, NJ). Sections were deparaffinized with xylene and rehydrated through a descending ethanol series before further use. The stained tissues were

characterized using a light microscope (BX 51, Olympus America Inc., San Diego, CA) and analyzed using Image Pro Plus v6.0 software (Media Cybernetics Inc., Silver Spring, MD) unless mentioned otherwise. For details on staining protocols, please refer to supplemental information.

2.2.1. Tartrate resistant acid phosphatase (TRAP) histochemistry

Deparaffinized serial sections were used for tartrate resistant acid phosphatase (TRAP) staining. In brief, the method included treating the rehydrated specimens with 0.2 M acetate buffer, a solution of 0.2 M sodium acetate and 50 mM L(+) tartaric acid (Sigma-Aldrich, St. Louis, MO) (Erlebacher and Derynck, 1996). After incubation at room temperature for 20 min, naphthol AS-MX phosphate and fast red TR salt were added, followed by incubation at 37 °C for 1 h with close monitoring under the microscope after the first half hour for bright red staining of osteoclastic activity. The stained sections were washed in deionized water, counterstained with hematoxylin and mounted with Immu-mount (ThermoScientific, Fremont, CA) for subsequent examination under a light microscope, as stated above. A survey of the distribution of TRAP stained osteoclasts in the periodontium of the 2nd molar was made using sections from 5 animals from experimental and control groups respectively.

2.2.2. Hematoxylin & eosin and picrosirius red staining

Sections were stained with hematoxylin (Fisher Scientific, Kalamazoo, MI) and eosin (Fisher Scientific, Kalamazoo, MI) (Carson 1990). Deparaffinized sections were stained with Sirius red F3B (C.I. 35,782) and picric acid (American MasterTech Scientific Co., Lodi, CA). Polarized light was used to enhance the birefringence of collagen to illustrate changes in collagen fiber orientation and birefringence intensity throughout the complex.

2.2.3. Alcian blue histochemistry

Deparaffinized serial sections were rehydrated through descending alcohols and placed in 1% alcian blue (American MasterTech Scientific Co., Lodi, CA) in 3% acetic acid solution at pH 2.5 for 30 min. After rinsing in running water, the sections were counterstained with nuclear-fast red solution (American MasterTech Scientific Co., Lodi, CA) for 5 min, followed by dehydration through ascending alcohols and xylene before mounting the sections with Permount (Fisher Scientific, Pittsburgh, PA).

2.2.4. Immunohistochemistry for biglycan (BGN) and bone sialoprotein (BSP) localization

Immunohistochemistry (IHC) of BGN was performed using an avidin-biotinylated peroxidase enzyme complex-based kit (Vectastain Elite: Vector Labs, Burlingame, CA) with 3,3′-diaminobenzidine (DAB) substrate (Sigma-Aldrich, St. Louis, MO) to produce a brown reaction product indicating antigen location. Deparaffinized and rehydrated sections were incubated in 80% methanol and 0.6% H_2O_2 to quench endogenous peroxidase. To retrieve antigen, trypsin digestion was performed for 10 min at room temperature in 0.1% trypsin, 0.1% $CaCl_2$, 20 mM Tris–HCl pH 7.8, followed by rinsing with deionized water 3 times for 5 min. Glycosaminoglycan (GAG) removal was next performed enzymatically in 35 mM Tris–HCl pH 7.4, 35 mM sodium acetate, and 15 mU/mL chondroitinase ABC (Seikagaku Biobusiness, Tokyo, Japan) for 1 h at 37 °C in a humidified chamber. Following antigen retrieval, sections were incubated with blocking buffer (1% normal donkey serum, 0.03% Triton X-100 in 1× phosphate-buffered saline (PBS)) for 60 min to prevent non-specific binding. The primary antibody (rabbit polyclonal anti-BGN antibody, LF-159, generously provided by Dr. Larry Fisher, NIH/NIDCR, Bethesda, MD) was applied on the sections at a dilution of 1:200 in blocking buffer and incubated overnight at 4 °C. The next day, the sections were washed in 0.1% Tween 20 in 1× PBS (PBST) and incubated for 30 min at room temperature with the secondary antibody (biotinylated anti-rabbit IgG antibody, PK-6101, Vector Labs, Burlingame, CA). Antigen–antibody complexes were visualized with DAB tetrachloride solution (Sigma, St. Louis, MO), washed in distilled water and counterstained with Gill hematoxylin (Fisher Scientific, Kalamazoo, MI), and rinsed in running water. Finally, the sections were dehydrated in ascending series of ethanol, cleared with xylene and mounted with Permount (Fisher Scientific, Pittsburgh, PA). Negative controls were obtained by the substitution of the primary antibodies with non-immunized rabbit IgG (Santa Cruz Biotechnology Inc., sc-2027, Santa Cruz, CA) and blank controls by omission of the primary antibodies. Condyles harvested from the same animals were used as positive controls. The sections were evaluated by a single examiner, blinded to the treatment assignment.

Bone sialoprotein (BSP) was assessed by immunohistochemistry (IHC) on a Leica Bond Max (Leica Microsystems, Inc., Buffalo Grove, IL) using the Bond Refine Detection System. Paraffin sections previously mounted on slides (Superfrost™ Plus Gold Slides, Thermo Fisher Scientific Inc., Waltham, MA) were deparaffinized, rehydrated, and surface decalcified for 10 min in Immunocal (Fisher Scientific, Pittsburgh, PA). All sections were blocked for endogenous peroxidases by immersion in 0.3% hydrogen peroxide in 30% methanol for 30 min at 25 °C. Epitope retrieval was achieved with citrate buffer (ER1, Bond Refine Detection System) for 60 min at 37 °C. Blocking of all sections was performed with the addition of Background Buster (Innovex Biosciences, Richmond, CA) for 30 min at 25 °C just prior to the addition of primary antibody. Monoclonal anti-BSP (mouse clone WVID1(9C5), Developmental Studies Hybridoma Bank, Iowa City, IA) was bound for 2 h at 25 °C at a 1:100 dilution (70 μg/mL). Mayer's hematoxylin (Bond Refine Detection System) was utilized as counterstain following the polymer-linked 3, 3′-diaminobenzidine (DAB, Bond Refine Detection System) secondary reaction. After counterstaining, all sections were dehydrated and sealed using DPX mountant (Sigma-Aldrich, St. Louis, MO). All experimental staining procedures were accompanied by control slides replacing primary antibody binding with buffer or mouse IgG isotype (Dako North America, Inc., Carpinteria, CA) to assess the level of non-specific staining.

2.2.5. Fluorescence microscopy

Experimental rats (N = 3) and control rats (N = 3) were given intraperitoneal injections with alternating alizarin red and tetracycline hydrochloride (both Sigma-Aldrich, St. Louis, MO, USA) on days 0, 3, 6, 9 and 12 of the procedure. According to the method used, 25 mg fluorochrome per kg body mass was diluted in 2% $NaHCO_3$ to a concentration of 0.01 mg/μl concentration of 0.01 mg/kg body mass (Luan et al., 2007). After harvest, maxillae were dissected, fixed in 4% paraformaldehyde overnight, and embedded in polymethylmethacrylate. Sagittal sections 10 μm thick were sliced on a rotary microtome (Leica RM2255, Leica microsystems, Wetzlar, Germany) using a tungsten carbide blade. Sections were viewed under Nikon 6D Ti-E conventional wide-field microscope (UCSF Nikon Imaging Facility, San Francisco, CA) equipped with an mCherry epifluorescence filter (ex = 560/55 nm, CWL/BW, em = 630/60 nm, CWL/BW) used to visualize Alizarin red fluorescent bands (abs. = 530–560 nm, em. = 580 nm), and Sapphire epifluorescence (filter: ex = 400/50 nm, CWL/BW, em = 515/50 nm, CWL/BW) used to visualize tetracycline HCL green fluorescent bands (abs.= 390–425 nm, em. = 525–560 nm).

2.3. Microprobe X-ray fluorescence (μ-XRF)

Ultrasectioned block specimens (0.64 mm thick) of an adapted bone-finger region, tooth and PDL were analyzed using μ-XRF microscopy at the Stanford Synchrotron Radiation Lightsource (SSRL) on beamline 2–3. Data acquisition was performed using constant parameters with an incident energy beam of 10 keV, dwell time of 25–50 ms per pixel, and a step size of 1 μm. The elemental concentrations were determined by calibration against a set of NIST traceable, thin film elemental X-ray fluorescence standards provided by Micromatter (Vancouver, Canada). Corrections to the area-based concentrations

(μg/cm^2) were performed based on the absorption and attenuation of both the incident (excitatory) X-ray photons (10 keV) and the various elemental fluorescence photons in the matrix.

2.4. Atomic force microscopy (AFM) imaging, AFM-based nanoindentation, and Raman spectroscopy

The topography of ultrasectioned surfaced-blocks was qualitatively analyzed using an atomic force microscope (Nanoscope III, Multimode; Bruker Corporation, Santa Barbara, CA) in contact mode under both dry and wet conditions. The ultrasectioned surface was scanned using a Si_3N_4 tip attached to a "V shaped" cantilever (Bruker Corporation) at a scanning frequency of 1.4 Hz. The nominal radius of curvature of the tip was less than 50 nm. Scanning under wet conditions was performed with the specimen and probe immersed in deionized water as previously described (Ho et al., 2004). Nanoscope III version 5.12r3 software (Bruker Corporation) was used for data processing.

2.4.1. AFM-based nanoindentation

Nanoindentation was performed on the ultrasectioned block specimens using an AFM attached to a load displacement transducer (Triboscope, Hysitron Incorporated, Minneapolis, MN). A sharp diamond Berkovich indenter with a conventional radius of curvature less than 100 nm (Triboscope, Hysitron Incorporated, Minneapolis, MN) was fitted to the transducer. Site-specific measurements across the adapted bone interface were made under wet conditions using a displacement control mode and a penetration depth of 500 nm, with a load, hold, and unload for 3 s each. Fused silica was used to calibrate the transducer under dry and wet conditions.

2.4.2. micro Raman spectroscopy

The chemical makeup of alveolar bone was probed with an ARAMIS Raman microscope (HORIBA Scientific, Santa Clara, CA), operated at 768 nm wavelength, with a 1200 grating, and at 50× magnification. Peak heights corresponding to phosphate (960 cm^{-1}, 1003 cm^{-1}, 1030 cm^{-1}) and amide III (1242 cm^{-1}) were compared to determine the mineral:matrix ratio.

3. Results

3.1. Mineralized zones, osteoclastic activity, and ratio of canal volume to total volume

Transverse micro-XCT images (Fig. 1) were used to determine the gross macroscale movements of the teeth relative to the bone after force application. The virtual sections demonstrated movement of the teeth in mesial direction, accompanied by an enlarged PDL-space on the distal side of roots (Fig. 1c), and decreased PDL-space on the mesial side. Resorption pits were observed in cementum opposite to bony finger extensions (Fig. 1d) (Fig. S1, Movies S1a, S1b, and S1c).

Active root resorption represented by the distribution of TRAP stained osteoclasts is shown in Fig. 1. Control specimens showed osteoclastic activity predominantly on the distal aspect of distal roots (Fig. 1e), while the experimental specimens exhibited TRAP activity on the mesial aspect of the mesial root (Fig. 1f). Resorption activity was highest on the bone–PDL interface but also undermining resorption was found occasionally in both experimental and control within the alveoli of the alveolar bone. No difference of resorption activity was found between the bones located in the apical or cervical half of the socket.

Alveolar socket and root morphology were consistent with signs of bone and cementum resorption. Micro-XCT images showed concave resorption pits, with diameters of approximately 50–100 μm, on the distal side of the root in control animals and on the mesial side of the experimental group. Similarly, resorption craters signifying root resorption were found on the mesial and distal sides of the roots in the experimental, while the control only exhibited natural root resorption on the distal side of the roots (Herber et al., 2012). There was no significant difference in the morphology of resorption pits in control or experimental groups, but the average size and total amount of resorption were higher on the mesial side of the mesial 2nd molar root compared to the experimental distal side and control. Additionally, based on transverse and longitudinal sections, resorption and growth occurred over an area/volume (white arrows, Fig. 1, Supplemental Movies S1a and S1b).

Average bone volume to total volume (BV/TV) and average canal volume to total volume (Ca.V/TV) in percentages are shown in Fig. 1g for control and experimental groups. The average Ca.V/TV for control and experimental groups was 25% and 40%, respectively, and that for BV/TV was 75% and 60%. Supplemental Movie S1c illustrates representative cubic subvolumes within 3D segmented, and Movies S1d and S1e illustrate bone and canal networks in control and experimental groups.

3.2. Cell morphology, tissue architecture, and biomolecular expressions at the PDL–bone and PDL–cementum attachment sites

Serial sections were stained and analyzed (Fig. 2). The hematoxylin and eosin stain was informative, in that varying cell morphology specifically at the PDL–bone attachment site, including increased capillaries, was observed within the PDL (Fig. S2). At the PDL–bone, there existed a zone of cells with an altered morphology and closer to the commonly known cuboidal shape of osteoblasts (Fig. 2). Additionally, the alternating but irregular layers of bone encroaching the PDL-space (Δ, Δ1, Δ2, Fig. 2c and d) stained pale pink were observed when compared to the existing bone (stars, Fig. 2c and d), and uniform layering in the controls (Fig. 2a and b).

PSR staining of control specimens displayed high birefringence indicating well organized collagen fibers and PDL inserts at both the cementum and bone interfaces (Fig. 2e and f), while the experimental group displayed birefringence only at the cementum–PDL interface, suggesting less organization at the bone–PDL site where strain-guided mineralization occurred (Fig. 2g and h). Finger-like extensions that appear green, indicating a lack of organized collagen, are noted protruding from the bone into the PDL-space. Hatched patterns suggest newly formed adapted alveolar bone is woven. Supplemental Movies S2a and S2b highlight the birefringence of control and experimental complexes through 360° rotation.

Alcian blue with nuclear fast red counterstaining (AB-NFR) was consistently positive in the bone, secondary cementum, and mantle dentin adjacent to secondary cementum (Fig. 2i, j, k and l), although the pale blue color was more intense in the control group (Fig. 2i and j). On the other hand, PDL, dental pulp and endosteal spaces exhibited pink cell nuclei and cytoplasm. Most interestingly, an intense blue staining was observed along the tip of finger-like bone protrusion at the bone–PDL interface in the experimental group (black arrows in Fig. 2k and l), which is absent in the control group. Large cuboidal cells (arrow heads in panel l) lining bone fingers are distinguished from small squamous cells in PDL and they are thought to be osteoblastic.

BGN was distributed uniformly throughout the PDL of the control group (Fig. 2m and n). BGN was also localized in the predentin layer, the bone lacunae and the cementum lacunae, irrespective of experimental condition. A strong positive reaction was observed along both the bone–PDL interface and cementum–PDL interface in the experimental group (black arrows in Fig. 2p). As seen in H&E (arrow heads in panel d) and AB-NFR (arrow heads in panel l), osteoblastic cells were along the bone-fingers, more specifically near the newly secreted BGN within what appears to be mineralizing matrix (note corresponding alcian blue stain in a similar region) (arrowheads in panel p).

The distribution of BSP was mainly associated with mineralized regions of the tissue such as cementum and alveolar bone as well as newly formed bony protrusions (Fig. 3). BSP was absent in the PDL. The light brown color in the new bone (NB, Fig. 3b2) indicated a lower content of BSP, suggesting an early stage of BSP deposition among other matrix proteins (Fig. 3e). A strong immunostaining was

observed in the cementum and alveolar bone, as indicated by the darker brown, suggesting that these mineralized regions could be mature in terms of matrix protein deposition (Fig. 3). Birefringence using polarized light indicated well-aligned collagen fibers at specific regions such as the PDL–cementum and PDL–bone interfaces (Fig. 3a3 and b3). The birefringence in the new bone region is sparse, suggesting that the collagen fibers do not have the same extent of organization (Fig. 3b3). This is consistent with the results obtained from PSR staining (Fig. 2g and h).

3.3. Mineralization through dynamic histomorphometry, microprobe X-ray fluorescence, and Raman microspectroscopy

Experimental specimens indicated an irregular mineralization pattern with finger-like protrusions on the distal side, and accompanying banding indicating enhanced mineralization of the finger-like regions (Fig. 4a and b). Fig. 4a highlights the increased rate of biomineralization in strained regions (boxed region) compared to less-strained regions (stars, Fig. 4a).

μ-XRF imaging within the adapted complex (Fig. 4d) illustrated highly variable mineral patterns with the presence of gradual and sharp mineral gradients (line profiles in Fig. 4d1 and d2). The distribution of Ca and Zn illustrated in μ-XRF maps within the bone, and at the bone–PDL–cementum interface demonstrated considerable heterogeneity as compared to μCT data, in which the mineral content was higher near the bone–PDL interface and near endosteal spaces. In μ-XRF imaging, similar patterns in elemental composition were observed with hot spots of Ca concentration appearing in mature bone (dark orange regions in Fig. 4d and dark red regions in Fig. 4d1 indicated by an unfilled diamond) and regions of reduced Ca concentration outlining both endosteal and vascular spaces of the adapted bone (yellow regions in Fig. 4d and yellow to green regions in Fig. 4d1). Elemental Zn was predominantly observed at the bone–PDL interface, outlining the newly developing bone fingers (yellow and green regions in Fig. 4d and d2), as well as in cement lines (yellow regions in Fig. 4d, asterisks in Fig. 4d2) and surrounding endosteal spaces. These local increases or decreases in calcium and zinc are illustrated by gradient profiles along lines in Fig. 4d1 and d2. Regions of new bone growth are highlighted in the Zn/Ca map in Fig. 4d3 and cement lines are further highlighted in the Zn/Ca map in Fig. 4d4 indicating that these areas within bone are higher in Zn and lower in Ca contents. It should be noted, that along the local compression side of the bone (the bone–PDL interface opposite the bone fingers), no bone finger protrusions were found in elemental maps (also none found in micro-XCT images), but resorption pits in bone were observed.

Raman spectroscopy line scans across regions of existing and bony finger-like protrusions, reported in Fig. 5a, showed an abrupt increase in the organic:inorganic composition of the bone from old into newer protruded bone. This finding exposed the nature of newly formed adapted bone as less mineralized compared to the original composition of mature bone.

3.4. Structural and mechanical properties as indicated by AFM Imaging and AFM-based nanoindentation

AFM imaging of the finger-like bone protrusions and their interface to existing bone under dry (Fig. 5a) and wet (Fig. 5b) conditions indicated higher hygroscopicity, representative of organic PDL-inserts, along the growth direction of finger-like protrusions (overlay Fig. 5b). Mechanical properties of the adapted bone protrusions were investigated with nanoindentation across the existing bone and protrusion interface. A gradual decrease in elastic modulus occurred over the interface, accompanied by a reduction in elastic modulus in the bulk of the finger-like bone protrusions.

4. Discussion

The objective of this study was to investigate the effect of amplified mechanical strain at the PDL–bone and PDL–cementum attachment sites and the resulting changes in physicochemical response to strain by mapping site-specific histochemical, elemental, and mechanical properties at the interfaces and within the tissues per se. Hence, the animal model presented herewith is only a version to prompt an active and abrupt stretch through strain amplification at the PDL–bone and PDL–cementum attachment sites. Results presented in this study validate the model as reported by others (Krishnan and Davidovitch, 2006; Meikle, 2006), in that; accentuated strains prompt rapid mineralization along the strained fibrils. However, it should be noted that the placement of the appliance can result in more chewing on the control side compared to the experimental side of the jaw. The result of this potential effect on the experimental side should also be taken into account.

Novel aspects include complementary maps of changes in biomolecule localization and physicochemical properties. It is these physicochemical changes that could have prompted the observed results, which are, mineral formation albeit shifting the bone–PDL–tooth fibrous joint into malfunction. While applied force in this study has led to gross tooth movements and perhaps shifts in rates of biomineralization, it is important to consider that bone modeling and drifts that prompted the form are an attempt to maintain optimum biomechanical function. As mentioned by Boyde, Frost and others, the waffle-like pattern of a woven bone and drifts in mineralization as seen using micro-XCT (Supplemental figures and all relevant figures), picrosirius red, and fluorochrome in this study are indicative of rapid mineralization of the strained organic matrix (Currey, 2002; Frost, 1994), and contains increased vasculature as seen in Figs. 1 and 2 as observed before (Frost, 1994). Interestingly, the appearance of the mineralized matrix was in the form of bony fingers indicating that certain fibers within the periodontal ligament will continue to be predominantly strained. This observation is counterintuitive, in that mineralization should occur along the overall structure of the strained PDL, a continuous “biphasic gasket” between the tooth and the alveolar socket. While we suspect that the spaces between the bony fingers are original endosteal spaces, it is possible that the rapid rate of intramembranous mineralization centers abut and can leave mineralizing free spaces (Boyde, 1980), thus enabling the buildup of the observed waffle-like structure of the new bone. However, what is minimally known is the “quality” of resulting woven bone, an essential characteristic that plays an integral role in maintaining organ function. Despite the need to locally regenerate tissue in response to a given impulse, it is important to note that the final outcome should be that the adapted complex that is, cementum, ligament and bone should accommodate functional loads throughout the life span of the organism. This implies that the tissue should acquire functional characteristics as it is regenerating in response to physical input and that knowledge about the resulting biochemical cues are necessary to prompt or resorb mineral with the ultimate goal of optimized biomechanics for organ function. Hence, the commonly and historically interrogated qualifiers such as mineral density, elemental composition, mechanical strength and homogeneity, are useful indicators to evaluate

Fig. 1. Transverse micro-XCT images of control (a) and experimental (b) specimens indicated the gross general movement of teeth in the mesial direction after applied force, accompanied by an increased distal PDL-space, and decreased mesial PDL-space. With higher resolution, (c) and (d) new bone formation in the form of bone-like fingers is noted extending into the PDL-space. TRAP staining for osteoclastic activity demonstrated a shift in resorption from predominantly mesial sites in (e) control specimens to distal sites in (f) the experimental group, contributing to the overall movement of teeth in the mesial direction. (g) The average bone volume fraction (BV/TV) and canal volume fraction (Ca.V/TV) were calculated from subvolumes with an average total volume (TV) of 0.11 mm^3. BV: alveolar bone volume; Ca.V: canal volume (blood vessels, endosteal spaces); TV: total volume, TV = BV + Ca.V. AB: alveolar bone, NB: new bone, T: tooth, C: cementum, PDL: periodontal ligament.

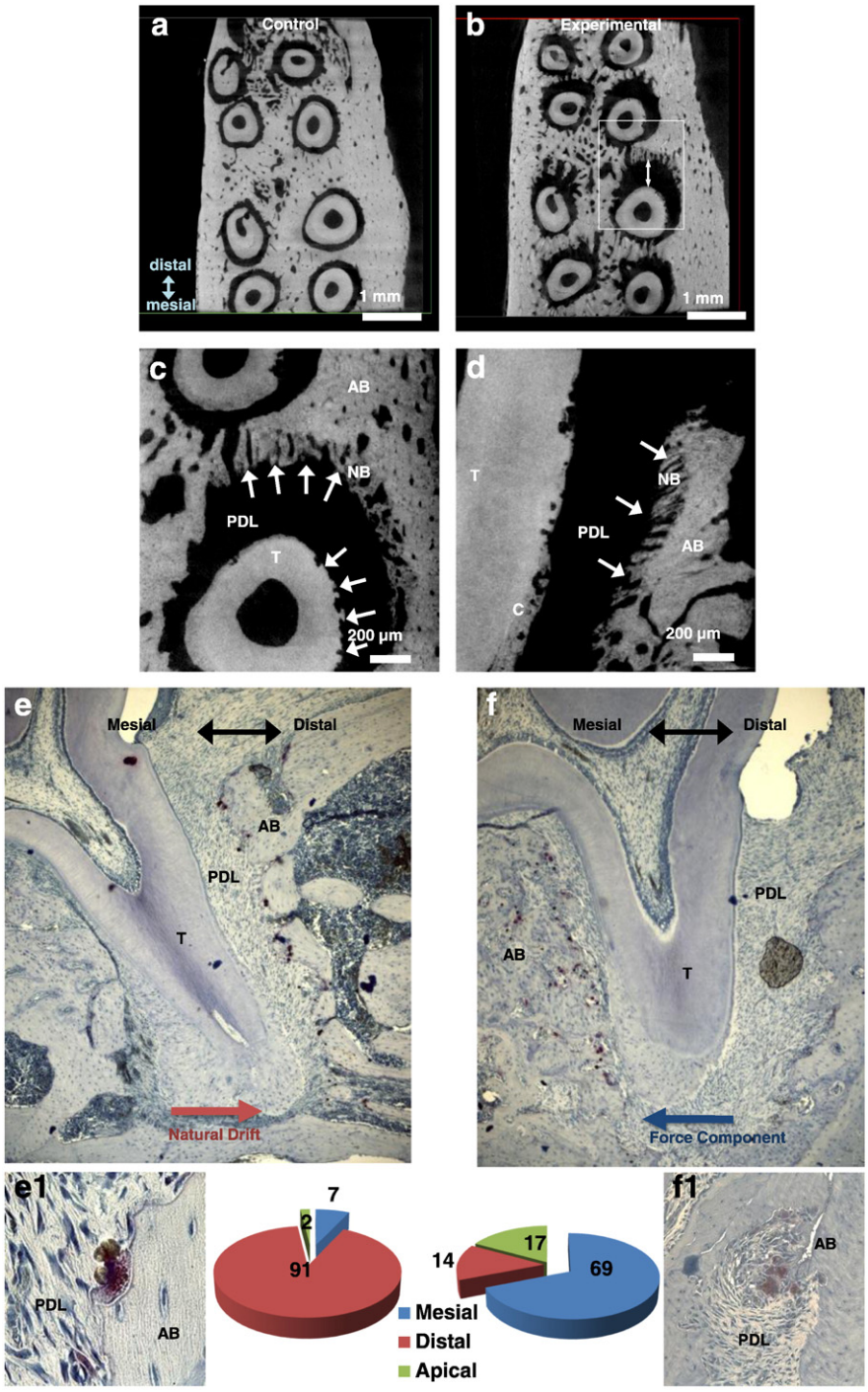

	Ave Ca.V/TV (%)	SEM	Ave BV/TV (%)	SEM
Experimental	39	14	61	14
Control	21	7	78	7

"functional quality" of regenerated tissues and the shift in physicochemical properties relative to the original lamellar bone. At this juncture, we postulate that the degree of variation in physicochemical properties between the adapted and original bone can potentiate elastic discontinuities, a stress concentration zone in alveolar bone during function. In previous works, such elastic discontinuities in the periodontium were proposed as potential precursors for of pathology and can disrupt normal joint function, i.e. shifting a joint toward malfunction (Ho et al., 2013; Hurng et al., 2011).

It is difficult to conceive that rapid mineralization can also prompt concomitant maturation of organic matrix and amorphous to crystalline phase transformation of mineral. Furthermore, the maturation of organic and inorganic is dependent on the effect of magnitude and rate of stimulus on an animal's age and gender. In studies on rat cortices, newer bone showed a 79% lower mineral to matrix ratio, and a higher CO_3:PO_4 ratio than the older bone, which was also accompanied by a lower hardness (Donnelly et al., 2010). Lower mineral indicated by X-ray attenuation and inorganic to organic ratio was reflected in our study, indicating that it is likely the newer formation in response to mechanical stimuli. In the absence of phase transformation information from amorphous to crystalline, the lower mineral content, yet heterogeneous due to lower and higher attenuation differences (Fig. 1, Movies S1 and S2), is likely responsible for the lower elastic modulus of these regions (Fig. 5). Rate at which a strong impulse is given often forms woven bone (Frost, 1994). The intense signal over a shorter time, the cascade of biochemical events, and the orchestration of biomolecules that is necessary to resemble the natural architecture are all prime candidates to induce "functional quality" to regenerating bone. The lower level of mineralization and resulting lower elastic modulus could be the lack of organization of the strain guided formations (PSR images Fig. 2g, h, Movies S2a and S2b) and higher polysaccharide composition at the mineralization front (Fig. 2k, l).

In understanding the biomineralization processes that underlie heterogeneities in the bone, it is first necessary to provide a perspective on how and why heterogeneity occurs within tissue types and interfaces. Hard tissues other than enamel having similar mechanisms of mineral formation (Nanci, 1999; Weiner and Traub, 1986), utilize collagen (the organic matrix) and an arsenal of noncollagenous matrix proteins (NCPs) to form intra- and extra-fibrillar mineral (Nanci, 1999). These formations, established during development and growth, contribute to structural integrity within each hard tissue per se and to structural integrity at the interfaces between the tissues. The net change in dynamic events of interfaces is relative and can affect an organ and its subsequent function. For example, both the dentin enamel junction and cementum dentin junction lie within the mineralized continuum of a tooth, but the PDL–bone and PDL–cementum functional interfaces are relatively more dynamic because of their role in transmitting and absorbing mechanical loads simply due to the anatomical location, and the nature of tooth movement in the alveolar socket. Functional loads in and of themselves affect the rate and occurrence of mineralization, but when compounded with extraneous forces, the enhanced effects at PDL–bone and PDL–cementum attachment sites often result in areas of accelerated tissue adaptation, the physicochemical properties of which are labeled in this study. Thus, the resulting mechanical and chemical heterogeneity could be a result of shift in magnitude and the rate at which the incremental load was applied. While this could be true and that bone remodels at a higher rate compared to cementum, what is not obvious from the images is that the adapted regions of the bone need not directly correspond to the changes at the PDL–cementum attachment site within the same geometric 2D plane. This effect is also observed when therapeutic loads are placed on the human teeth (Reitan and Rygh, 1994). In order to highlight the effect of bone growth, and a corresponding affected cementum, several movies are included within this manuscript (Supplemental movies). It is to be noted that a one-to-one correlation between affected bone and cementum cannot be made within the same 2D plane. We speculate that this could be due to either of the following two reasons, or a combination of the two: 1. Function could affect the 3D strain profile within the complex on to which an appliance was placed. 2. The placement of the appliance not only prompted lateral translation, but could have torqued the tooth about the interradicular bone. Regardless, future work related to organ-level biomechanical studies can provide insights about the overall tooth movement in the socket following adaptation of the complex.

With this bioengineered model, it is possible to investigate vectorial biomineralization due to the innate mechano-responsive nature of the PDL. It is postulated that the rapid shift in strain, and the abundance of noncollagenous proteins at the strained attachment site could have reduced the thermodynamic barrier for nucleation (nucleation barrier) causing a significant change in the rate of mineralization (Mann, 2001). The amplified strains felt by cells at the attachment sites due to eccentric placement of mechanical loads, prompted a shift in turnover rates of the extracellular matrix. The resulting shifts in turnover rates of the matrices interspersed with cell at the attachment sites can result in heterogeneous nucleation along the dominant vector of the applied force. Moreover, the rapid rate of mineralization was also suggested by the nodules noted in fluorochrome images (Fig. 4), further suggesting that the applied strain initiated their irregular formation, and contrary to the regular mineral apposition in controls (not shown).

Concepts related to biomineralization and functional adaptations in the skeletal bone are not new. In fact, some of the founding principles on the bone formation, such as Wolff's law, are based on the response of bone arrangement to mechanical stimuli (Wolff, 1892). Among the competing theories in orthopedic based studies, Liskova et al. demonstrated the inability of cells to sense the difference between tension and compression, or rather that irrespective of the type of applied force bone formation resulted (Liskova and Hert, 1971). Sandy et al. postulated that cells cannot differentiate between compression and tension forces, and that the bone formation under orthodontic force is governed by cytokines produced locally (Sandy et al., 1993). It has been long known that the growth of the alveolar bone can also be a result of the bending of the alveolar wall in response to the pull produced by Sharpey's fibers (Melsen, 1999). Indeed, polarized light microscopy complemented with AFM imaging clearly demonstrated that the organization of Sharpey's fibers or the PDL-inserts (Figs. 2 and 5), were closely related to the formation of adapted bone under tension by such fibers. The higher density of cellular clusters at the interface between original and newly (Figs. 2 and 5) formed bone suggests strained PDL in initiating mineralization. The higher molecular weight proteoglycans identified with AB-NFR and low molecular weight proteoglycans mapped by BGN were observed. Biglycan in general is one of the players in the cascade of events leading to osteoinductivity (Parisuthiman et al., 2005) and its upregulated expression surrounding the bone-finger protrusions suggests the induction of higher osteoblastic activity. Moreover, the noted change in the morphology of the cells specifically at the attachment sites corroborates with the notion that strain amplification prompts semiautonomous regions to promote tissue adaptation in response to demands placed by extraneous loads. H&E stained images (Fig. 2c, d) also highlight increased large cuboidal osteoblastic cells lining bone-fingers. These mechanisms can prompt a structure similar to that observed in the woven bone, with increased vascularity, but altered mineral density. Therefore, from a clinical perspective one should consider the possibility that protracted loading, whether due to functional demands or clinical intervention, may shift the natural balance of zones that reside closer to PDL–cementum and PDL–bone outer walls. These zones that contain multicellular networks can form semiautonomous regions over time and cause uncontrolled or erratic mineralization, potentially at the expense of whole organ function. BSP is a putative non-collagenous proteins (NCPs) closely associated with normal and pathologic mineralization (Fisher et al., n.d.). The functions of BSP are rather versatile presumably because of the structural features on BSP's backbone containing acidic groups binding calcium ions and arginine–glycine–aspartate (RGD) sequence helping the

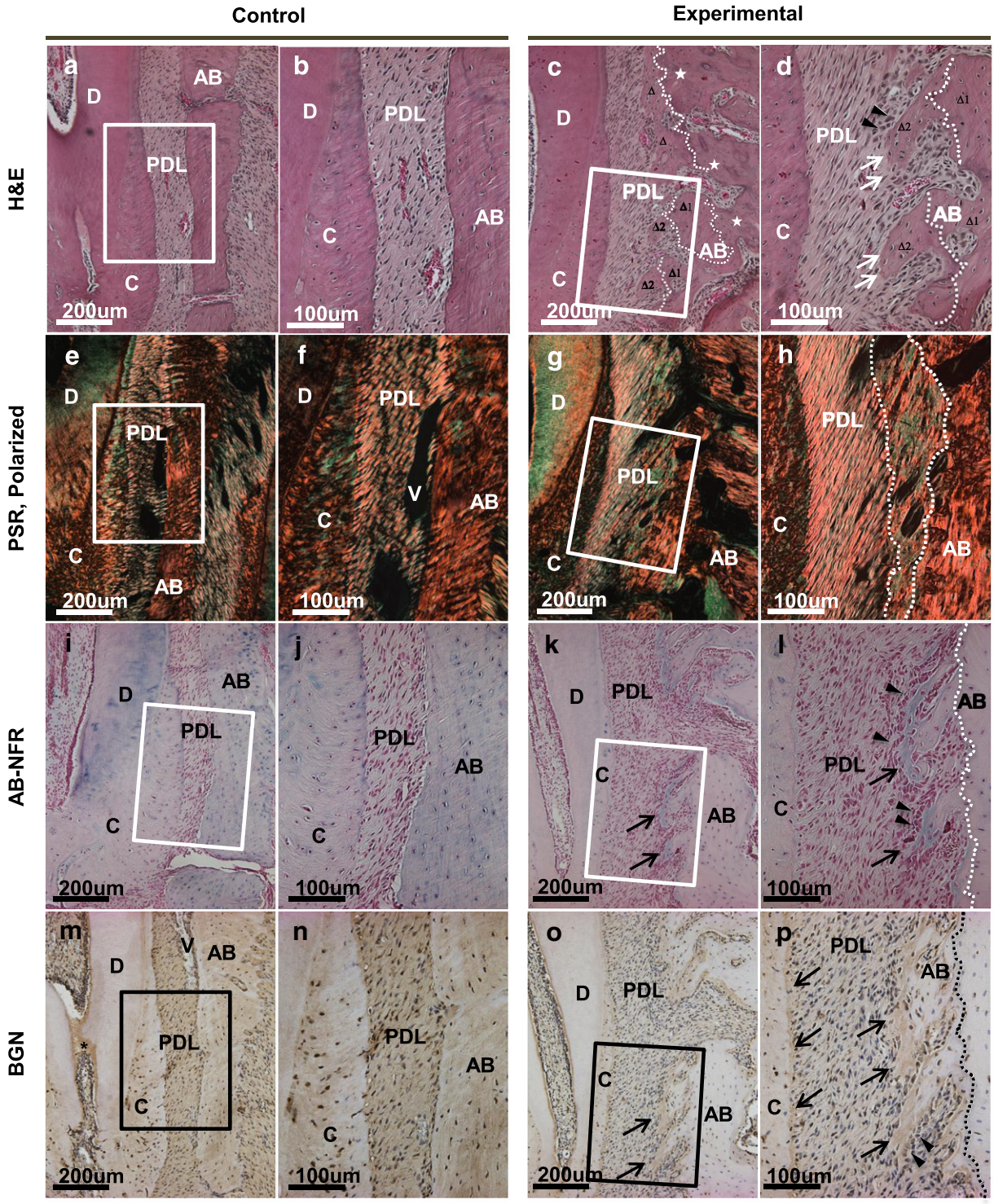

Fig. 2. Tension-dominating regions in control groups and experimental groups showing hematoxylin and eosin (H&E) staining (a–d), picrosirius red (PSR) staining visualized under polarized light microscope (e–h), alcian blue counterstained with nuclear fast red (AB-NFR) (i–l), and immunohistochemistry for biglycan (BGN) (m–p). These are all tension-dominating regions, that is, mesial side of maxillary second molar in control groups and distal side of maxillary second molar in experimental groups. Bone–PDL interface in control group is smooth, well-demarcated and highly-birefringent (a, b), whereas experimental group shows finger-like bone protrusions (white arrows in panels of c, d), which is correspondent to the greenish-orange colored bone adjacent to the bone–PDL interface (g, h). In the control group, high birefringence of collagen is shown both at bone–PDL and cementum–PDL interfaces indicating the existence of well-organized Sharpey's fibers (e, f). In the experimental group, however, collagen fibers appear to be more stretched but they show poor quality of organization at bone–PDL interface and the alveolar bone adjacent to the interface (indicated by greenish-orange color, enclosed in dotted lines in panels of g, h). AB-NFR staining reveals a layer of acidic polysaccharides-rich zone on the front line of finger-like bone protrusions in experimental group (k, l), which is absent in control group (i, j). BGN is strongly expressed along both bone–PDL and cementum–PDL interfaces in experimental group (black arrows in panels of o, p), but in control group (m, n), BGN is distributed evenly in periodontal ligament and also positive in predentin (asterisk in panel of m). Enclosed boxes in panels a, c, e, g, l, k, m and o (original magnification, ×100) represent regions shown at higher magnification in panels b, d, f, h, j, l, n and p (original magnification, ×200), respectively. Alveolar bone (AB), periodontal ligament (PDL), cementum (C), dentin (D) new bone (NB), and blood vessel (V).

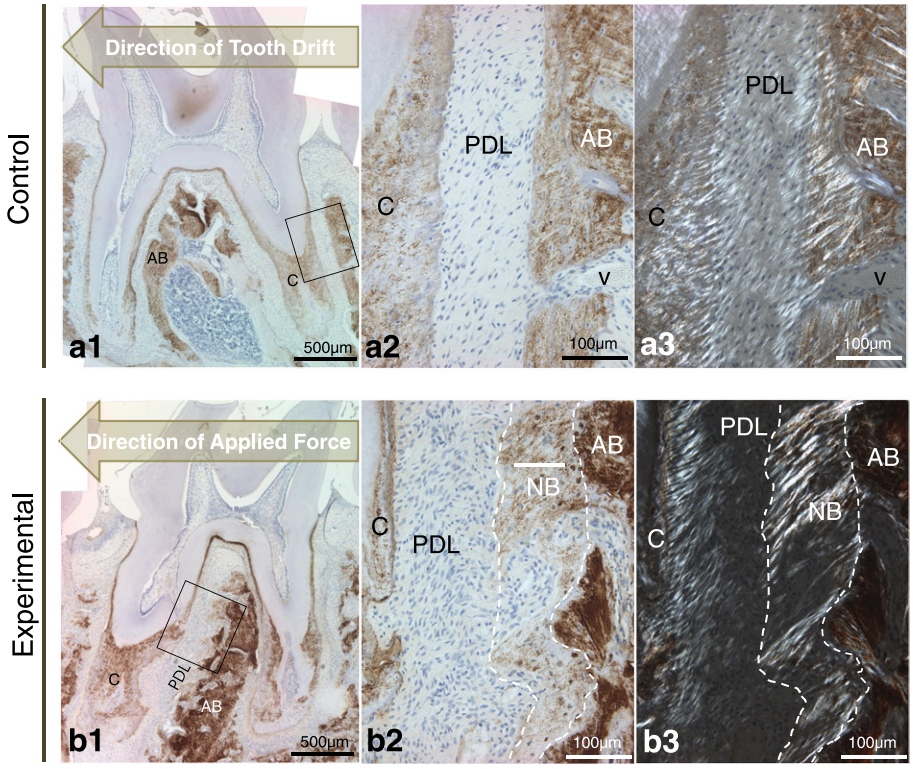

Fig. 3. Immunohistochemistry for bone sialoprotein (BSP) of control and experimental groups. BSP was evenly distributed in primary and secondary cementum as well as alveolar bone in control group (a1). Similar morphological appearance was noticed in experimental groups. However, there are some distinct features to be noticed. Some light-brown stains appear to be associated with bone protrusions (marked with dotted lines in b2, b3) whereas the parent bone shows a strong immunostaining with a mottled appearance. Both control and experimental groups show that BSP is absent in PDL region. This is in accordance with immunolocalization results reported by McKee and Nanci [Ref Cooper et al., 2006]. From polarized microscopic images, the birefringence is more prominent in the cementum–PDL interface and alveolar bone, suggesting the presence of many well aligned collagen fibers. Some birefringence is also noticed in the newly formed bone region for experimental group, indicating strain-mediated modeling process of the bone when subject to strain. These observations suggest strain prompt new bone formation from alveolar bone region at the PDL–bone interface. Enclosed boxes in panels a1 and b1 represent regions, which are tension dominating and shown at higher magnification in panels a2 and b2. Panels a3 and b3 are correspondent to a2 and b2 respectively, when analyzer and polarizer are applied. AB: alveolar bone, PDL: periodontal ligament, C: cementum, NB: new bone, V: blood vessel.

regulation of cell behaviors. BSP molecules also have a collagen-binding domain (Scott and Stockwell, 2006). The interaction between BSP and collagen facilitates apatite formation (Puxkandl et al., 2002). The RGD motif of the BSP backbone suggests BSP may play an important role for osteoblast differentiation (Fisher et al., n.d.; Yamauchi and Sricholpech, 2012). Among other NCPs, the expression of BSP is well correlated with mineralization events. Therefore, BSP would be an ideal indicator of mineralization events in this study. In the strain amplified region, the new bone formation is confirmed by the presence of BSP and collagen fibers while the PDL was free of BSP (Fig. 3). Apparently, the matrix deposition and modification such as the accumulation of BSP and mineralization of strained ECM are a result from regulated cell behavior and its interaction with the small integrin binding ligand N-linked glycoprotein, BSP. The data clearly indicates the capacity of strain in potentiating cellular events at the PDL–bone and PDL–cementum sites, the attachment sites of disparate materials (soft and hard).

While the presence of BSP and BGN at the respective interfaces is an indicator of osteoid-like and cementoid-like matrices, the presence of elemental Zn may be an indicator of increased local activity of matrix metalloproteinases necessary for accelerated tissue turnover prior to mineralization (Pemmer et al., 2013; Roschger et al., 2013). The unique patterns of Zn may be a temporal marker of mineralization of organic matrices. Previously, the presence of Zn has shown no direct correlation to Ca content (Pemmer et al., 2013) and was independent of the mineral deposition rate in the bone (Murray and Messer, 1981). However, other studies do indicate a correlation of Zn and bone mineralization, illustrating that Zn can have a stimulatory effect on mineralization (Yamaguchi et al., 1987) or inhibitory effects at reduced levels (Maser et al., 2008; Ryz et al., 2008). These conflicting results may be clarified by breaking down and classifying the different types of biomolecular events in which elemental Zn plays a role. This classification could be based on the turning on of the genetic switch that triggers the molecular events and the resulting specific patterns. For example, it could be that the shift in strain at the PDL–bone attachment sites prompt higher turnover of the tissue, thus resulting in increased MMP (matrix metalloproteinases) activity that contains elemental Zn. It was shown that adaptation prompted by disease and external loads contain increased Zn amounts in the cementum and bone (Maser et al., 2008; Roschger et al., 2013). In this study, we have observed Zn in the softer tissue PDL, and we speculate that it could be due to increased PDL turnover rate due to a shift in mechanical strain. However, whether Zn can further prompt matrix mineralization remains to be a hypothesis.

Understanding the mechanisms governing strain guided mineralization is not simple. Based on results from this study, it is the assemblage of simultaneous and complementary processes that guide mineralization in the direction of force vector. A hypothetical model depicting the events associated with the strain guided mineralization at the bone–PDL interface is given in Fig. 6. The collagen fibers and/or fibrils at PDL are under tension with shear between the fibers and fibrils upon the application of force on the teeth (Fig. 6a). The proteoglycan bridging neighboring collagen fibrils help distribute load. During tension, the collagen fibrils are straightened and stretched subsequently along with the induction of shear between fibrils and collagen molecules that makeup the fibrils. The neighboring collagen molecules may also glide against each other, widening the gap zone associated with staggered molecular packing of collagen (Fig. 6b) (Scott and Stockwell,

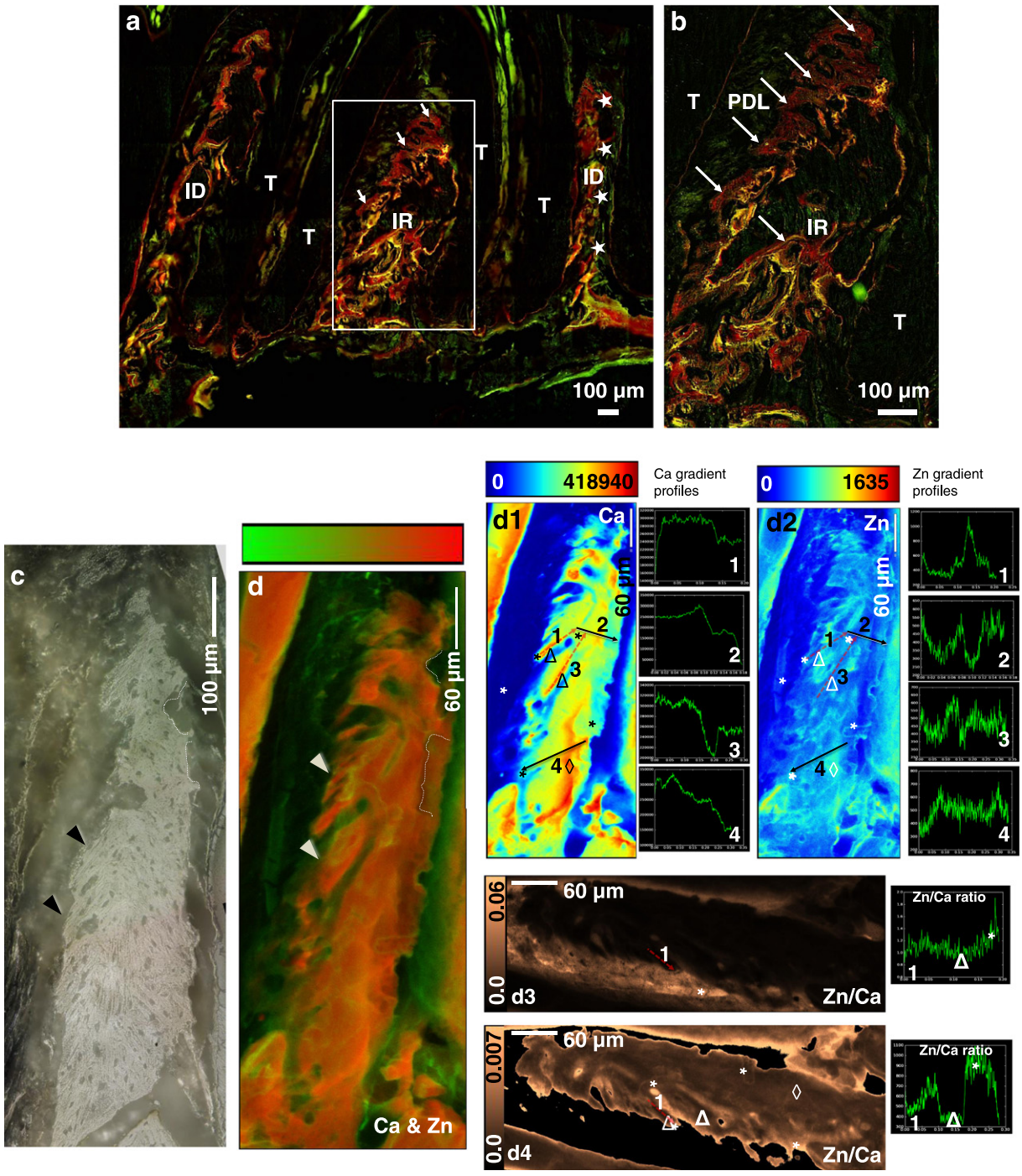

Fig. 4. Fluorochrome images of experimental (a, b) groups reveal irregular patterns of mineralization. Control specimens displayed regular banding patterns which indicated a progressing biomineralization front. Experimental specimens indicate much less organized mineralization and nodules or finger-like protrusions of biomineralization in regions experiencing tension, for example the boxed region, compared to unstrained regions marked by *. Upon closer inspection of D, the strained region shows increased mineralization consistently surrounding blood vessel or endosteal spaces as marked by arrows. The vessels appear to be elongated along the direction of strain, and such a mechanical cue may be contributing to the enhanced mineral formation in their vicinity. Gradients in microprobe XRF elemental mapping are illustrated and are correlated with structural features as indicated by light microscopy technique. A bicolor elemental map for calcium and zinc signals shown in (d) and a corresponding light microscope image in (c). Gradients in (d) show calcium and zinc in existing bone (orange to dark orange), zinc only in areas of new bone growth within PDL (green), and new bone-finger regions high in zinc yet low in calcium (yellow) which correspond to cement lines (also observed in controls) and active sites of remodeling surrounding bone finger protrusions. AB: alveolar bone, NB: new bone, T: tooth, PDL: periodontal ligament.

2006). Inside the collagen fibrils, the telopeptides of collagen molecules are typically cross-linked with other neighboring collagen molecules (Puxkandl et al., 2002). These covalent crosslinks between the collagen molecules can hinder further slippage of molecules and also increase the overall stiffness of collagen fibrils. Meanwhile, cells attached to the matrix through small integrin binding ligand N-linked glycoprotein such as BSP are also regulated by the strain in collagen of the PDL. As suggested in Fig. 6c and d, the force acting on the cytoskeletal components of cells triggers a series of downstream processes including gene expression, protein synthesis, ECM deposition and mineralization as well as osteoclast recruitment (Yamauchi and Sricholpech, 2012). As very little is known, a number of theories were extrapolated from similar tissues such as ligaments and tendons, and *in vitro* studies which provided analogous insights to the observed *in vivo* events in this study.

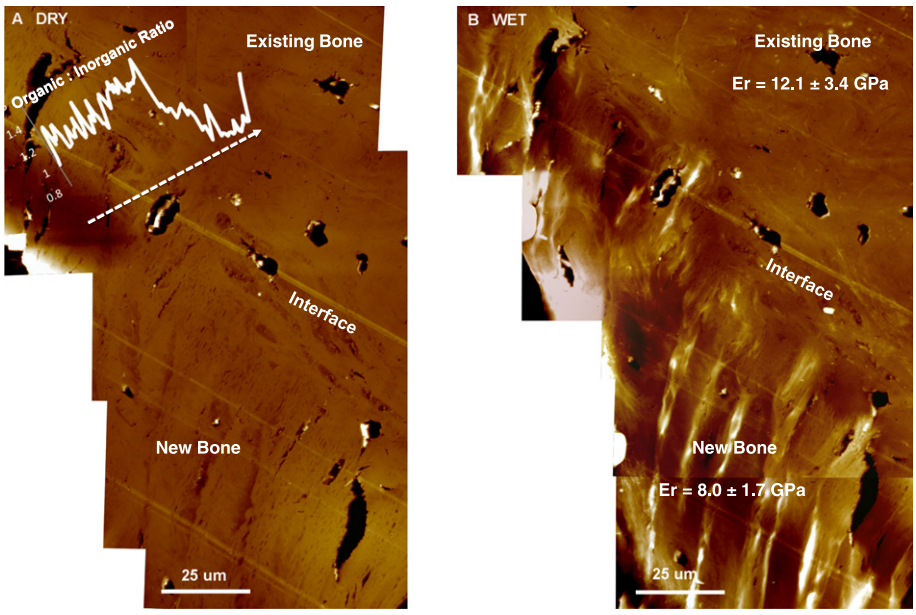

Fig. 5. The interface between existing and new bone (identified as finger-like protrusions) as imaged with AFM under dry (A) and hydrated (B) conditions. Notice the highly populated cell-density along the interface or genesis site of adapted bone formation, indicative of a strongly differentiating zone. Collagen fiber inserts display increased hygroscopicity under hydrated conditions with their orientation consistent with the finger-like growth direction. Raman spectroscopy, overlain in A, indicated the higher organic:inorganic ratio in newly formed protrusions versus existing bone. Nanoindentation values in B support the finding of higher organic components in the newer bone by the lower reduced elastic modulus versus existing bone.

5. Conclusion

The present study enabled investigation of biomineralization effects in the bone–PDL–tooth complex such as tooth movement, resulting deformation of the PDL in three-dimensions, as well as correlation to physicochemical properties of tissues. The results provide evidence for strain-guided or vectorial biomineralization in the complex, characterized by physiologically reversed resorption patterns and protruding bone formations with altered physicochemical properties into the PDL-space. These results suggest that the rates of adaptation are increased at the richly differentiating semiautonomous zones of the PDL entheses, and therefore susceptible to controlled modulation or

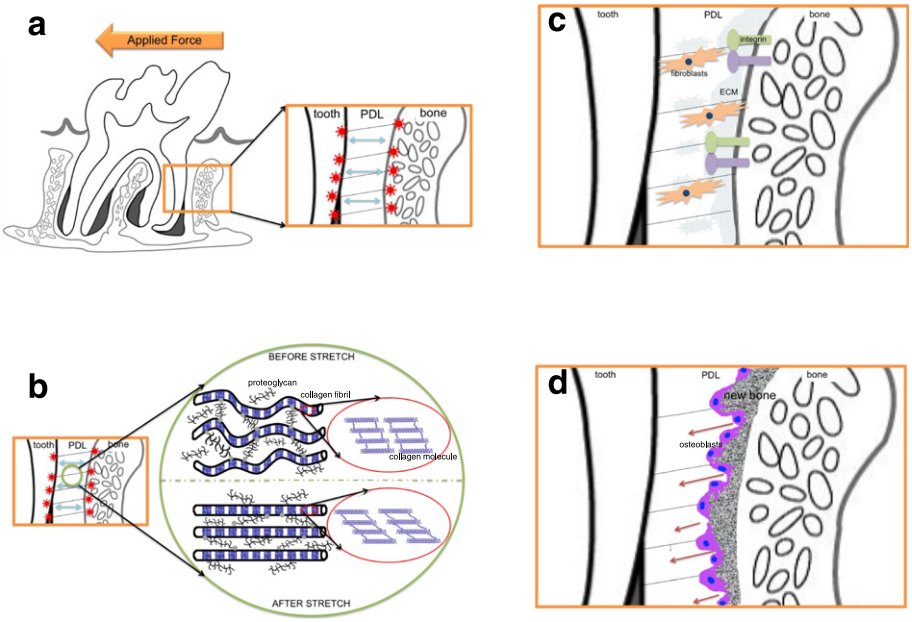

Fig. 6. A model describing potential events at the PDL–bone functional attachment site of the complex is highlighted in this figure. (a) At macroscale, mechanical stimuli such as tensile stress cause straightening and elongation of the collagen fibers PDL. (b) At microscale, collagen fibers are made from collagen fibril bundles while collagen fibrils consist of staggered packed collagen molecules. Tension of collagen fibers exerts stretching of collagen fibrils (thin rods with blue and white bands). The proteoglycans bridging collagen fibrils allow the interfibrillar transmission of load. Sliding of collagen molecules (ribbons of blue triple helix) provides additional displacements and widens the gap zone of a collagen fibril. However, the intermolecular crosslinking bonds prevent the further slippage. The proteoglycans between collagen fibrils and the covalent crosslinks between collagen molecules all contribute to the mechanical behavior of collagen fibers and benefit the structural integrity during the tension. (c) Apparently, cells embedded in the ECM of PDL are subject to tension. ECM transmits the strain resulted from external force on teeth to cytoskeletal components of cells in PDL. Such mechanical stimuli trigger a cascade of intracellular and extracellular processes to modify the ECM such as regulated gene expression, protein synthesis, matrix deposition and mineralization. Meanwhile, the matrix signaling facilitates recruitment of osteoclasts. (d) New bone formation and remodeling takes place at the PDL–bone interface, suggesting an active cell behavior such as differentiation and ECM production. Regulated mineralization of ECM occurs as a result of such strained guided adaption at PDL–bone interface.

modulation toward pathology under exacerbated conditions. An altered biomechanics of the entire bone–PDL–tooth complex resulting from orthodontic forces highlight the clinical relevance of this work.

Supplementary data to this article can be found online at http://dx.doi.org/10.1016/j.bonr.2015.04.002.

Acknowledgments

The authors acknowledge funding support from NIH/NIDCR R00DE018212 (SPH), NIH/NIDCR-R01DE022032 (SPH), NIH/NIDCR T32 DE07306, NIH/NCRR S10RR026645, (SPH) and Departments of Preventive and Restorative Dental Sciences and Orofacial Sciences, UCSF; Faculty of Engineering, McMaster University (Hamilton, Canada) (KG). The authors thank Linda Prentice of the Histology Core Facility, and The UCSF Biomaterials and Bioengineering Micro-CT Facility, Department of PRDS, UCSF for their services with the tissue preparation and imaging. Additional thanks to Andrew Jang, DDS, for his assistance in generating the movies related to micro-XCT data. Assistance from national facilities through user based program was provided by Stanford Synchrotron Radiation Lightsource (SSRL), SLAC National Accelerator Laboratory, Stanford University, CA and The Molecular Foundry, Lawrence Berkeley National Laboratory, Berkeley, CA. Work at the SSRL was supported by the U.S. Department of Energy under contract number DE-AC02-76SF00515. Work at the Molecular Foundry was supported by the Office of Science, Office of Basic Energy Sciences, of the U.S. Department of Energy under Contract No. DE-AC02-05CH11231. The WVID1(9C5) monoclonal antibody against BSP developed by M. Solursh and A. Franzen was obtained from the Developmental Studies Hybridoma Bank developed under the auspices of the NICHD and maintained by the University of Iowa, Department of Biology, Iowa City, IA.

References

Beertsen, W., McCulloch, C.A., Sodek, J., 1997. The periodontal ligament: a unique, multifunctional connective tissue. Periodontology 2000 (13), 20–40.

Boyde, A., 1980. Electron microscopy of the mineralizing front. Metab. Bone Dis. Relat. Res. 2, 69–78.

Carter, D.R., Fyhrie, D.P., Whalen, R.T., 1987. Trabecular bone density and loading history: regulation of connective tissue biology by mechanical energy. J. Biomech. 20, 785–794. http://dx.doi.org/10.1016/0021-9290(87)90058-3.

Carter, Y., Thomas, C.D.L., Clement, J.G., Cooper, D.M.L., 2013. Femoral osteocyte lacunar density, volume and morphology in women across the lifespan. J. Struct. Biol. 183, 519–526. http://dx.doi.org/10.1016/j.jsb.2013.07.004.

Cooper, G.M., Singhal, V.K., Barbano, T., Wigginton, W., Rabold, T., Losken, H.W., Siegel, M.I., Mooney, M.P., 2006. Intracranial volume changes in craniosynostotic rabbits: effects of age and surgical correction. Plast. Reconstr. Surg. 117, 1886–1890. http://dx.doi.org/10.1097/01.prs.0000218845.70591.7e.

Currey, J.D., 2002. The structure of bone tissue. Bones: Structure and Mechanics.

Donnelly, E., Boskey, A.L., Baker, S.P., van der Meulen, M.C.H., 2010. Effects of tissue age on bone tissue material composition and nanomechanical properties in the rat cortex. J. Biomed. Mater. Res. 92, 1048–1056. http://dx.doi.org/10.1002/jbm.a.32442.

Erlebacher, A., Derynck, R., 1996. Increased expression of TGF-B2 in osteoblasts results in osteoporosis-like phenotype. J. Cell Biol. 132, 195–210.

Fisher, L.W., Torchia, D.A., Fohr, B., Young, M.F., Fedarko, N.S., n.d. Flexible Structures of SIBLING Proteins, Bone Sialoprotein, and Osteopontin. Biochem. Biophys. Res. Commun. 280, 460–465.

Frost, H.M., 1994. Wolff's Law and bone's structural adaptations to mechanical usage: an overview for clinicians. Angle Orthod. 64, 175–188. http://dx.doi.org/10.1043/0003-3219(1994)064<0175:WLABSA>2.0.CO;2.

Herber, R.-P., Fong, J., Lucas, S.A., Ho, S.P., 2012. Imaging an Adapted Dentoalveolar Complex. Anatomy Research International, pp. 1–13 http://dx.doi.org/10.1155/2012/782571.

Ho, S.P., Goodis, H., Balooch, M., Nonomura, G., Marshall, S.J., Marshall, G., 2004. The effect of sample preparation technique on determination of structure and nanomechanical properties of human cementum hard tissue. Biomaterials 25, 4847–4857. http://dx.doi.org/10.1016/j.biomaterials.2003.11.047.

Ho, S.P., Kurylo, M.P., Grandfield, K., Hurng, J., Herber, R.-P., Ryder, M.I., Altoe, V., Aloni, S., Feng, J., WEbb, S., Marshall, G.W., Curtis, D., Piennatta, P., Hayter, J.A., 2013. The plastic nature of the human bone–periodontal ligament–tooth fibrous joint. Bone 57 (2), 455–467. http://dx.doi.org/10.1016/j.bone.2013.09.007.

Hurng, J.M., Kurylo, M.P., Marshall, G.W., Webb, S.M., Ryder, M.I., Ho, S.P., 2011. Discontinuities in the human bone–PDL–cementum complex. Biomaterials 32, 7106–7117. http://dx.doi.org/10.1016/j.biomaterials.2011.06.021.

Jang, A.T., Lin, J.D., Seo, Y., Etchin, S., Merkle, A., Fahey, K., Ho, S.P., 2014. In situ compressive loading and correlative noninvasive imaging of the bone–periodontal ligament–tooth fibrous joint. J. Vis. Exp. http://dx.doi.org/10.3791/51147.

Krishnan, V., Davidovitch, Z., 2006. Cellular, molecular, and tissue-level reactions to orthodontic force. Am. J. Orthod. Dentofac. Orthop. 129, 469.e1–469.e32. http://dx.doi.org/10.1016/j.ajodo.2005.10.007.

Lin, J.D., Özcoban, H., Greene, J.P., Jang, A.T., Djomehri, S.I., Fahey, K.P., Hunter, L.L., Schneider, G.A., Ho, S.P., 2013. Biomechanics of a bone–periodontal ligament–tooth fibrous joint. J. Biomech. 46, 443–449. http://dx.doi.org/10.1016/j.jbiomech.2012.11.010.

Liskova, M., Hert, J., 1971. Reaction of bone to mechanical stimuli. 2. Periosteal and endosteal reaction of tibial diaphysis in rabbit to intermittent loading. Folia Morphol. (Warsz) 19, 301–317.

Lu, H.H., Thomopoulos, S., 2013. Functional attachment of soft tissues to bone: development, healing, and tissue engineering. Annu. Rev. Biomed. Eng. 15, 201–226. http://dx.doi.org/10.1146/annurev-bioeng-071910-124656.

Luan, X., Ito, Y., Holliday, S., Walker, C., Daniel, J., Galang, T.M., Fukui, T., Yamane, A., Begole, E., Evans, C., Diekwisch, T.G.H., 2007. Extracellular matrix-mediated tissue remodeling following axial movement of teeth. J. Histochem. Cytochem. 55, 127–140. http://dx.doi.org/10.1369/jhc.6A7018.2006.

Mann, S., 2001. Biomineralization: Principles and Concepts in Bioinorganic Materials Chemistry. Oxford University Press.

Maser, R.E., Stabley, J.N., Lenhard, M.J., Owusu-Griffin, P., Provost-Craig, M.A., Farquhar, W.B., 2008. Zinc intake and biochemical markers of bone turnover in type 1 diabetes. Diabetes Care 31, 2279–2280. http://dx.doi.org/10.2337/dc08.

Meikle, M.C., 2006. The tissue, cellular, and molecular regulation of orthodontic tooth movement: 100 years after Carl Sandstedt. Eur. J. Orthod. 28, 221–240. http://dx.doi.org/10.1093/ejo/cjl001.

Melsen, B., 1999. Biological reaction of alveolar bone to orthodontic tooth movement. Angle Orthod. 69, 151–158. http://dx.doi.org/10.1043/0003-3219(1999)069<0151:BROABT>2.3.CO;2.

Murray, E.J., Messer, H.H., 1981. Turnover of bone zinc during normal and accelerated bone loss in rats. J. Nutr. 111, 1641.

Nanci, A., 1999. Content and distribution of noncollagenous matrix proteins in bone and cementum: relationship to speed of formation and collagen packing density. J. Struct. Biol. 126, 256–269. http://dx.doi.org/10.1006/jsbi.1999.4137.

Parfitt, A.M., Drezner, M.K., Glorieux, F.H., Kanis, J.A., Malluche, H., Meunier, P.J., Ott, S.M., Recker, R.R., 1987. Bone histomorphometry: standardization of nomenclature, symbols, and units. Report of the ASBMR Histomorphometry Nomenclature Committee. J. Bone Miner. Res. 2, 595–610. http://dx.doi.org/10.1002/jbmr.5650020617.

Parisuthiman, D., Mochida, Y., Duarte, W.R., Yamauchi, M., 2005. Biglycan modulates osteoblast differentiation and matrix mineralization. J. Bone Miner. Res. 20, 1878–1886. http://dx.doi.org/10.1359/JBMR.050612.

Pemmer, B., Roschger, A., Wastl, A., Hofstaetter, J.G., Wobrauschek, P., Simon, R., Thaler, H.W., Roschger, P., Klaushofer, K., Streli, C., 2013. Spatial distribution of the trace elements zinc, strontium and lead in human bone tissue. Bone 57, 184–193. http://dx.doi.org/10.1016/j.bone.2013.07.038.

Puxkandl, R., Zizak, I., Paris, O., Keckes, J., Tesch, W., Bernstorff, S., Purslow, P., Fratzl, P., 2002. Viscoelastic properties of collagen: synchrotron radiation investigations and structural model. Philos. Trans. R. Soc. B Biol. Sci. 357, 191–197. http://dx.doi.org/10.1098/rstb.2001.1033.

Qian, L., Todo, M., Morita, Y., Matsushita, Y., Koyano, K., 2009. Deformation analysis of the periodontium considering the viscoelasticity of the periodontal ligament. Dent. Mater. 25, 1285–1292. http://dx.doi.org/10.1016/j.dental.2009.03.014.

Reitan, K., Rygh, P., 1994. Biomechanical principles and reactions. In: Graber, T.M., Vanarsdall, R.L. (Eds.), Orthodontics: Current Principles and Techniques. Mosby Year Book, Inc., St. Louis, Missouri, pp. 159–161.

Roschger, A., Hofstaetter, J.G., Pemmer, B., Zoeger, N., Wobrauschek, P., Falkenberg, G., Simon, R., Berzlanovich, A., Thaler, H.W., Roschger, P., Klaushofer, K., Streli, C., 2013. Differential accumulation of lead and zinc in double-tidemarks of articular cartilage. Osteoarthr. Cartil. 21 (11), 1707–1715. http://dx.doi.org/10.1016/j.joca.2013.06.029.

Ryz, N.R., Meddings, J.B., Taylor, C.G., 2008. Long-chain inulin increases dendritic cells in the Peyer's patches and increases ex vivo cytokine secretion in the spleen and mesenteric lymph nodes of growing female rats, independent of zinc status. BJN 101, 1653. http://dx.doi.org/10.1017/S000711450812342X.

Sandy, J.R., Farndale, R.W., Meikle, M.C., 1993. Recent advances in understanding mechanically induced bone remodeling and their relevance to orthodontic theory and practice. Am. J. Orthod. Dentofac. Orthop. 103, 212–222.

Scott, J.E., Stockwell, R.A., 2006. Cartilage elasticity resides in shape module decoran and aggrecan sumps of damping fluid: implications in osteoarthrosis. J. Physiol. Lond. 574, 643–650. http://dx.doi.org/10.1113/jphysiol.2006.108100.

Weiner, S., Traub, W., 1986. Organization of hydroxyapatite crystals within collagen fibrils. FEBS Lett. 206, 262–266.

Wolff, J., 1892. Das Gesetz der Transformation der knochen. A. Hirschwald, Berlin (This monograph was translated to English and was published by Springer-Verlag in 1986).

Yamaguchi, M., Oishi, H., Suketa, Y., 1987. Stimulatory effect of zinc on bone formation in tissue culture. Biochem. Pharmacol. 36, 4007–4012. http://dx.doi.org/10.1016/0006-2952(87)90471-0.

Yamauchi, M., Sricholpech, M., 2012. Lysine post-translational modifications of collagen. Essays Biochem. 52, 113–133. http://dx.doi.org/10.1042/bse0520113.